Supplementary information for "Bicircular high-harmonic spectroscopy reveals dynamical symmetries of atoms and molecules"

Denitsa Baykusheva, Md Sabbir Ahsan, Nan Lin, and Hans Jakob Wörner*

Laboratorium für Physikalische Chemie, ETH Zürich,

Vladimir-Prelog-Weg 2, 8093 Zürich, Switzerland

(Dated: February 16, 2016)

*hwoerner@ethz.ch; www.atto.ethz.ch

I. PHASE-MATCHING CALCULATIONS

The aim of the current section is to establish the extent to which phase-matching effects affect the absolute intensity of a given high harmonic as well as the disparity between adjacent $3q$+1 vs. $3q$+2 orders. A recent publication [1] stipulated that selective enhancement (or suppression) of left- or right-circularly polarized high harmonics can be achieved by tuning phase-matching parameters. The present experiment, however, is conducted in a different experimental geometry. In contrast to using a gas cell or a capillary, HHG in a thin gas jet is deliberately designed to minimize phase-mismatch. In the following we examine the contribution of extrinsic phase effects to the HHG spectra of helium and neon.

The molecular beam is generated by supersonic expansion through a pulsed-valve nozzle (Parker) with an orifice diameter of $\varnothing$ 250μm. The applied backing pressure was 6 bars. The focus intersects the beam at a distance of $\lesssim 1$ mm downstream the nozzle. Using the known relations [2] for (continuous) supersonic gas expansion, the pressure in the interaction region can be estimated as 2.4 mbar for the two species. These numbers correspond to a particle density of $\approx 1.4 \cdot 10^{18}$ cm^{-3}. The estimated rotational temperature in the generation region is 13 K. We note that these are conservative estimates, the real interaction region pressure will be slightly lower due to the fact that the valve is operated in a pulsed regime, while the equations are derived under the assumption of continuous flow. Following the approach introduced in [1], we first estimate the effective index change Δn_i ($i = \{1, 2\}$) for each of the two drivers individually by using the modified equation:

$$\Delta n_i = \left(\frac{\lambda_i k_i}{2\pi} - 1 \right) = P \left[(1 - \eta)(n_i - 1) - \frac{1}{2\pi} \eta N_{\mathrm{atm}} r_{\mathrm{e}} \lambda_i^2 \right], \tag{1}$$

where P, η and r_{e} denote the pressure of the gas, the ionization fraction and the classical electron radius, respectively. λ_i and k_i denote the wavelength and the k-vectors of each driver, while N_{atm} is the number density of the respective species at atmospheric pressure. The fit parameters for the Sellmeier equation needed for estimation of the effective refractive index n_i are taken from [3]. This expression has the same form as the phase mismatch equations given in Refs. ([4–6]), except for the omission of the modal term associated with the hollow-core-fibre experimental setup.

The most crucial and subtle part of the phase-matching calculation concerns the estimation of the ionized gas fraction (η). One approach would be to approximate the ionization

fraction with the time-dependent norm of the wave-function obtained from the TDSE calculations (Fig. S2). For the peak intensities / pulse durations consistent with the experimental estimations, one obtains: $\eta_{\mathrm{He}} \approx 0.008$ and $\eta_{\mathrm{Ne}} \approx 0.0353$. The phase mismatch $\Delta k_{3q\pm1}$ for a given pair of harmonics associated with the integer multiple q is obtained via:

$$\Delta k_{3q\pm1} = -\frac{2\pi}{\lambda_1}\left[q\left(\Delta n_1 + 2\Delta n_2\right) \pm \Delta n_1\right]. \tag{2}$$

The ratios of the coherence lengths $L_{\mathrm{coh}} = \pi/\Delta k$ estimated with the aid of the above quantity and the calculated absorption lengths $L_{\mathrm{abs}} = 1/(\rho\sigma)$ [7] yield the result displayed in panel A of Fig. S1. These results, alongside with the calculated coherence lengths displayed in Fig. S1 B (where $L_{\mathrm{coh}} >> 1$ mm for He and Ne), lead to the conclusion that phase matching effects can be ignored for He and Ne in the relevant range of harmonic energies. The experimental observations were found to be robust with respect to variation of phase-matching parameters such as backing pressure or laser-beam aperture size.

Another propagation effect that needs to be accounted for is the Gouy phase shift. In the current experiment, the effect of the Gouy phase shift across the focus is minimized by placing the focus several mm in front of the jet.

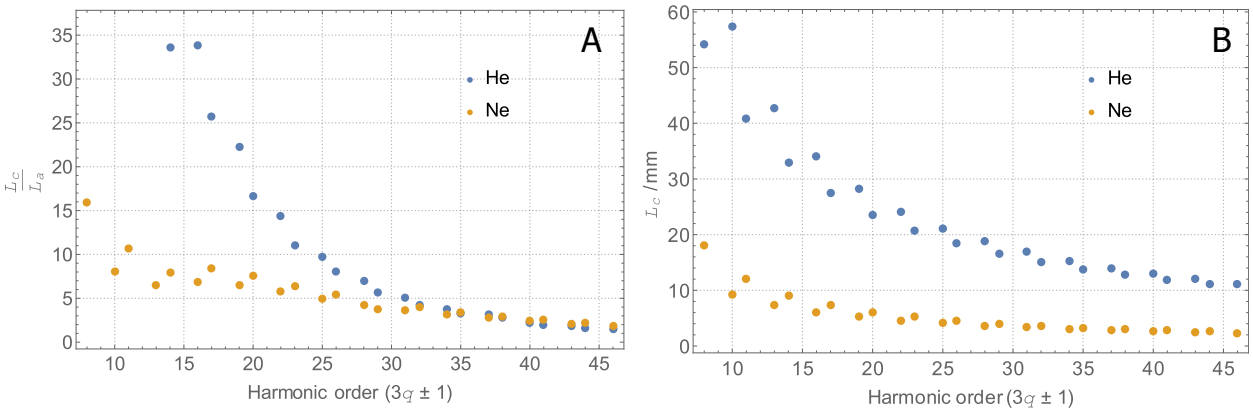

FIG. S1: Panel A: Estimated ratio of the coherence lengths vs. absorption lengths for harmonic energies relevant for the current experiment. A ratio $L_{\mathrm{c}}/L_{\mathrm{a}} > 5$ indicates that the output HHG flux corresponds to 90 % of the flux under ideal phase-matching conditions. Panel B: Estimated coherence lengths of the high harmonics generated in He and Ne.

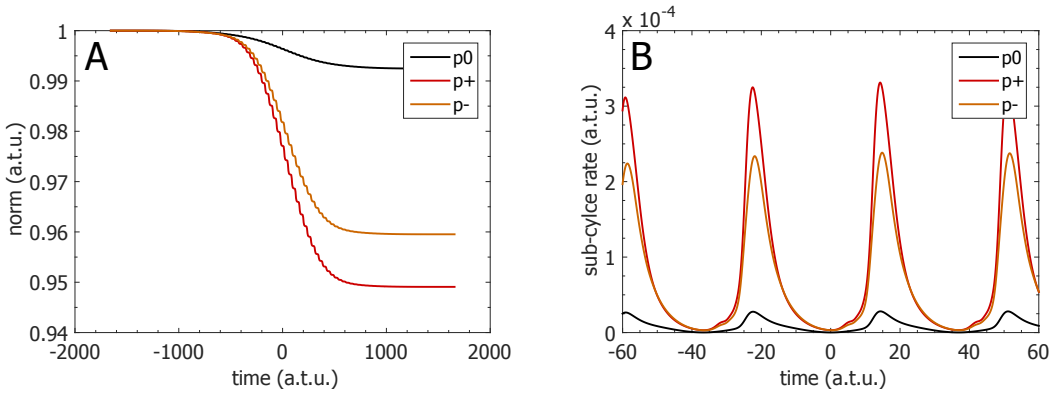

FIG. S2: TDSE results for the ionization fraction for each of the p-orbitals of Ne in a bicircular field ($I_\omega = 3.0 \times 10^{14}$ W/cm^2 and $I_{2\omega} = 1.8 \times 10^{14}$ W/cm^2). Panel A: Time-dependent norm of the wavefunction as a function of time. Panel B: Differential ionization rate for several half-cycles around the maximum of the pulse envelope.

II. DETAILS ON THE TDSE CALCULATION

In this work, electron dynamics in bi-chromatic bi-circular counter-rotating fields are investigated by numerically solving the time-dependent Schrödinger equation $\hat{H}(t) = -\frac{1}{2}\frac{\partial^2}{\partial r^2} + \frac{l(l+1)}{2r^2} + V_{\text{eff}}(r) + \vec{r}\cdot\vec{E}(t)$ for the helium and neon atoms in the single-active-electron (SAE) approximation. The wavelengths of the two drivers are set to 800 nm (RCP) and 400 nm (LCP), resulting in an electric field $\vec{E}(t) = E_\omega f(t)(\cos(\omega t)\hat{x} + \sin(\omega t)\hat{y}) + E_{2\omega} f(t)(\cos(2\omega t + \Delta\varphi)\hat{x} - \sin(2\omega t + \Delta\varphi)\hat{y})$, $f(t)$ being a $\cos^2$-pulse envelope. Since the azimuthal symmetry of the electron dynamics is lifted upon interaction with the bi-circular field, the full three-dimensional problem needs to be addressed. For this aim, we use the pseudo-spectral method described in detail in [8] and expand the single-electron wave-function in terms of radial and spherical harmonic functions as:

$$\Psi(r,\theta,\phi) = \sum_{lm} \frac{R_l(r,t)}{r} Y_{lm}(\theta,\phi). \tag{3}$$

The radial coordinate $r \in [0, r_{\max}]$ is discretized on a non-equidistant Legendre-Lobatto quadrature via the mapping: $r(x) = L\frac{1+x}{1-x+\alpha}$, $x \in [-1,1]$, with L being an arbitrary constant and $\alpha = 2L/r_{\max}$. A Legendre quadrature ($l = 0, 1, \ldots, l_{\max}-1$) is used for the latitude variable θ, while ϕ is discretized on an equidistant Fourier grid. The wave-function is propagated using the split-operator approach outlined in [9]. Ionization is modelled by placing an absorbing boundary.

Typical values for the time step, intensity and angular momentum cut-off are summarized in Tab. 1. The results were tested for convergence with respect to the number of grid points, time step and angular momentum basis size.

intensity 1	I_ω	3.0×10^{14} W/cm^2
intensity 2	$I_{2\omega}$	1.8×10^{14} W/cm^2
time step	dt	0.01 – 0.1 a.u.
cut-off radius	$r_{\max}$	300 a.u.
cut-off l	$l_{\max}$	64
radial grid size	$N_{\max}$	300-450

TABLE I: Parameters for the TDSE calculation.

The model potentials $V_{\text{eff}}(r)$ for He and Ne are taken from [10]. For argon, we use the model potential described in [11]. For the atoms with p-orbital symmetry, the relative delay between the two fields $\Delta\varphi$ is varied over one cycle and the harmonic emission is averaged over the resulting contributions.

III. DETAILED TREATMENT OF THE PHOTORECOMBINATION STEP

In the following, we explain the observed asymmetry in the intensity distribution of harmonic orders $3q+1$ and $3q+2$ in terms of a simple analytical model that does not rely on a full numerical solution of the TDSE. The point of departure of our analysis is the link between photoionization phenomena and the last step of the HHG process - radiative recombination. The principle of detailed balance dictates that the two processes are time-reversed counterparts of each other. This relationship has been exploited to reveal information of electronic structure encoded in the HHG spectra [12].

Treating the photorecombination step of the HHG process as a time-reversed photoionization involves one specific aspect concerning the mutual orientation of the photoelectron momentum axis ($\hat{\boldsymbol{k}}$), the electric field polarization axis ($\hat{\boldsymbol{n}}$) and the laboratory-frame quantization axis ($\hat{\boldsymbol{Z}}$). In linearly polarized fields, the emitted XUV field is parallel to the common axis of polarization and field quantization, i. e. $\hat{\boldsymbol{k}} \parallel \hat{\boldsymbol{n}} \parallel \hat{\boldsymbol{Z}}$. For HHG driven by bicircular fields, we set the quantization axis ($\hat{\boldsymbol{Z}}$) parallel to the propagation axis (which we denote by

$\hat{\boldsymbol{n}}$) of the field. In this case, the electron trajectories are confined to the 2D-plane orthogonal to the propagation direction, which implies that $\hat{\boldsymbol{k}} \perp \hat{\boldsymbol{Z}} \parallel \hat{\boldsymbol{n}}$.

We describe the photorecombination step as time-reversed *coherent* photoionization from the p_+- and p_--orbitals of Ne initiated by a circularly polarized field. As in the main text, we assume an RCP fundamental (ω) and an LCP second harmonic (2ω). In this description, the intensity of harmonic orders $(3q \pm 1)$ is proportional to:

$$I_{3q\pm1} \propto \left| \sqrt{c_+} \langle \Psi^+_{\boldsymbol{k}} | \hat{r}_\pm | 2p_+ \rangle + \sqrt{c_-} \langle \Psi^+_{\boldsymbol{k}} | \hat{r}_\pm | 2p_- \rangle \right|^2, \tag{4}$$

whereby $\hat{r}_+$ and $\hat{r}_-$ are the components of the dipole moment operator in spherical tensor form ($\hat{r}_\pm = \sqrt{\frac{4\pi}{3}} Y_{1\pm1}$). The coefficients $c_\pm$ in eq. (4) represent the ionized fractions of the $p_\pm$ orbitals. In the current model, we use the estimations $c_+ \approx 0.51$ and $c_- \approx 0.49$ from the TDSE calculation described in the preceding section.

The radial part $R_{21}(r)$ of the bound neon $|2p\rangle$ orbital is obtained by diagonalization of the field-free Hamiltonian including the model SAE potential on a Legendre-Lobatto radial grid. The total wavefunction is then constructed as $|2p_\pm\rangle = R_{21}(r) Y_{1\pm1}(\hat{\boldsymbol{r}})$. The scattering continuum states $\Psi^+_{\boldsymbol{k}}$ are normalized on the wave-vector scale ($\frac{1}{\sqrt{k}}$) and are expressed in terms of the partial-wave expansion:

$$\Psi^+_{\boldsymbol{k}} = \frac{1}{\sqrt{k}} \sum_{l=0}^{\infty} \sum_{m=-l}^{l} i^l \mathrm{e}^{i(\delta_l + \sigma_l)} R_{kl}(r) Y_{lm}(\hat{\boldsymbol{r}}) Y^*_{lm}(\hat{\boldsymbol{k}}). \tag{5}$$

The radial parts $R_{kl}(r)$ of the continuum wave functions as well as the phase shifts consisting of a Coulomb (σ_l) and a short range (δ_l) part are obtained using a Numerov algorithm. The continuum functions are normalized by matching them asymptotically at large distances to a potential consisting of a short-range potential and an ionic Coulomb tail. Insertion of this ansatz into eq. (4) leads to the following expressions for the individual matrix elements:

$$\langle \Psi_{\boldsymbol{k}}^{+}|\hat{r}_{-}|2p_{+}\rangle = \sqrt{\frac{9}{k}}\mathrm{e}^{-i(\delta_0+\sigma_0)}\langle R_{k0}|r|R_{21}\rangle \begin{pmatrix} 0 & 1 & 1 \\ 0 & 0 & 0 \end{pmatrix}\begin{pmatrix} 0 & 1 & 1 \\ 0 & -1 & 1 \end{pmatrix} Y_{00}(\hat{\boldsymbol{k}})$$
$$+ \sqrt{\frac{15}{k}}\mathrm{e}^{-i(\delta_2+\sigma_2)}\langle R_{k2}|r|R_{21}\rangle \begin{pmatrix} 2 & 1 & 1 \\ 0 & 0 & 0 \end{pmatrix}\begin{pmatrix} 2 & 1 & 1 \\ 0 & -1 & 1 \end{pmatrix} Y_{20}(\hat{\boldsymbol{k}}) \quad (6)$$

$$\langle \Psi_{\boldsymbol{k}}^{+}|\hat{r}_{-}|2p_{-}\rangle = \sqrt{\frac{15}{k}}\mathrm{e}^{-i(\delta_2+\sigma_2)}\langle R_{k2}|r|R_{21}\rangle \begin{pmatrix} 2 & 1 & 1 \\ 0 & 0 & 0 \end{pmatrix}\begin{pmatrix} 2 & 1 & 1 \\ 2 & -1 & -1 \end{pmatrix} Y_{2\,-2}(\hat{\boldsymbol{k}}) \quad (7)$$

$$\langle \Psi_{\boldsymbol{k}}^{+}|\hat{r}_{+}|2p_{-}\rangle = \sqrt{\frac{9}{k}}\mathrm{e}^{-i(\delta_0+\sigma_0)}\langle R_{k0}|r|R_{21}\rangle \begin{pmatrix} 0 & 1 & 1 \\ 0 & 0 & 0 \end{pmatrix}\begin{pmatrix} 0 & 1 & 1 \\ 0 & 1 & -1 \end{pmatrix} Y_{00}(\hat{\boldsymbol{k}})$$
$$+ \sqrt{\frac{15}{k}}\mathrm{e}^{-i(\delta_2+\sigma_2)}\langle R_{k2}|r|R_{21}\rangle \begin{pmatrix} 2 & 1 & 1 \\ 0 & 0 & 0 \end{pmatrix}\begin{pmatrix} 2 & 1 & 1 \\ 0 & 1 & -1 \end{pmatrix} Y_{20}(\hat{\boldsymbol{k}}) \quad (8)$$

$$\langle \Psi_{\boldsymbol{k}}^{+}|\hat{r}_{+}|2p_{+}\rangle = \sqrt{\frac{15}{k}}\mathrm{e}^{-i(\delta_2+\sigma_2)}\langle R_{k2}|r|R_{21}\rangle \begin{pmatrix} 2 & 1 & 1 \\ 0 & 0 & 0 \end{pmatrix}\begin{pmatrix} 2 & 1 & 1 \\ -2 & 1 & 1 \end{pmatrix} Y_{22}(\hat{\boldsymbol{k}}). \quad (9)$$

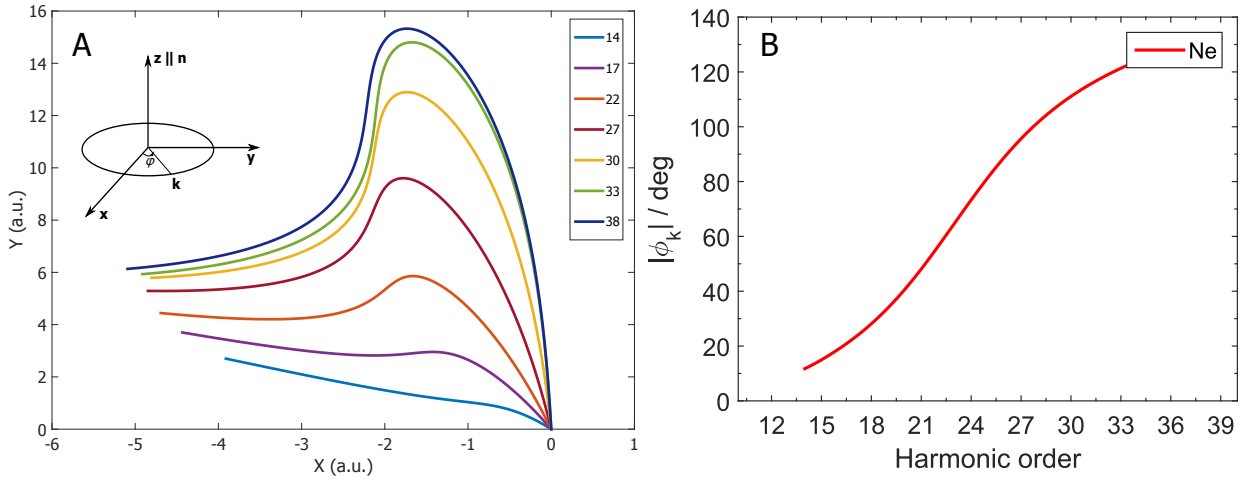

FIG. S3: Panel A: Real-time electron trajectories for a Ne atom calculated for the intensities employed in the experiment. The individual paths do not commence at the origin but rather at the tunnel exit. Nevertheless, they all return to the origin for the recombination event. The inset illustrates the coordinate system convention adopted in this section. Panel B: Calculated relative recombination angles ϕ_k for Ne.

An important question concerns the recombining electron trajectory, which enters the above matrix elements via the angle-dependent part $Y_{lm}(\hat{\boldsymbol{k}}) \equiv Y_{lm}(\theta_k, \phi_k)$. The choice $\hat{\boldsymbol{k}} \perp$

$\hat{\boldsymbol{Z}} \parallel \hat{\boldsymbol{n}}$ implies that $\theta_k = \pi/2$ and the recolliding electron trajectory is expressed via the azimuthal angle ϕ_k (cp. also the inset in Fig. S3 A). In general, the choice of the space-fixed $\hat{\boldsymbol{x}}$- and $\hat{\boldsymbol{y}}$-axes is arbitrary. In the following, we choose to identify the $\hat{\boldsymbol{x}}$-axis (which sets $\phi = 0$) as the axis corresponding to the instantaneous ionization direction of the electron. In order to obtain the tunneling ionization trajectory as well as the relative recollision angles, we employ the semiclassical saddle-point method outlined in [13]. The thereby obtained complex-valued stationary points $(t_{\mathrm{ion}}, t_{\mathrm{rec}}, \boldsymbol{p}_{\mathrm{st}})$ can be interpreted as instants of ionization, recombination and stationary momentum, respectively, and used to calculate the quantum trajectories contributing to a given harmonic order.

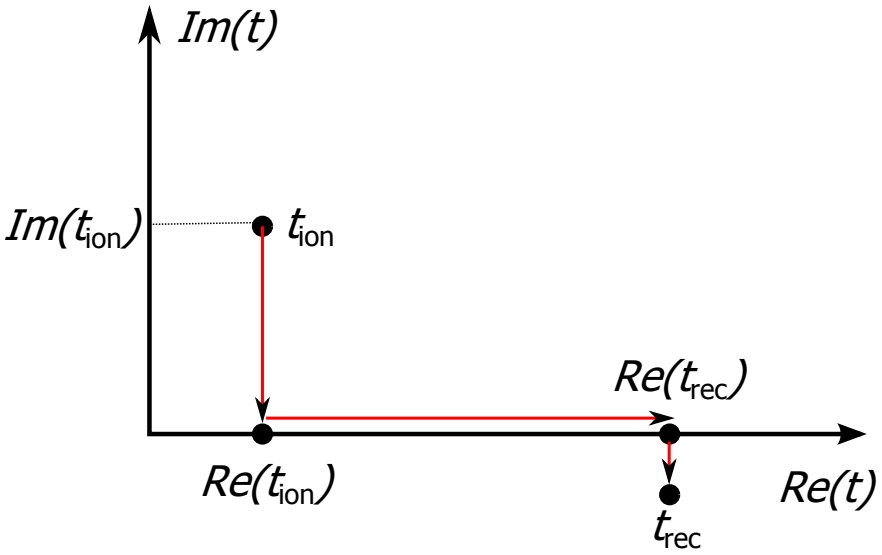

FIG. S4: Illustration of the integration path used to determine the electron trajectories. Details are given in the text.

We calculate the real-space electron trajectories $\boldsymbol{r}(t)$, a selection of which are displayed in Fig. S3 A, by integrating the corresponding equations of motion from t_{ion} to t_{rec} first along the imaginary time axis (from t_{ion} to $\Re\{t_{\mathrm{ion}}\}$) and subsequently along the real axis (from $\Re\{t_{\mathrm{ion}}\}$ to $\Re\{t_{\mathrm{rec}}\}$, neglecting the small imaginary part $\Im\{t_{\mathrm{rec}}\}$ associated with the electron return time. This integration path is illustrated in Fig. S4 . As a consequence of the imaginary part of t_{ion}, the "starting" point of each trajectory is not exactly at the origin, but several atomic units away from it, compatible with the tunneling ionization mechanism. We calculate the relative angles ϕ_k between the instantaneous "ionization" and "recollision" axes by evaluating the direction of the electron kinetic momentum vector at the "tunnel

exit" and at the recombination event. As evident from Fig. S3 B, typical values of ϕ_k span the range $30 - 140°$.

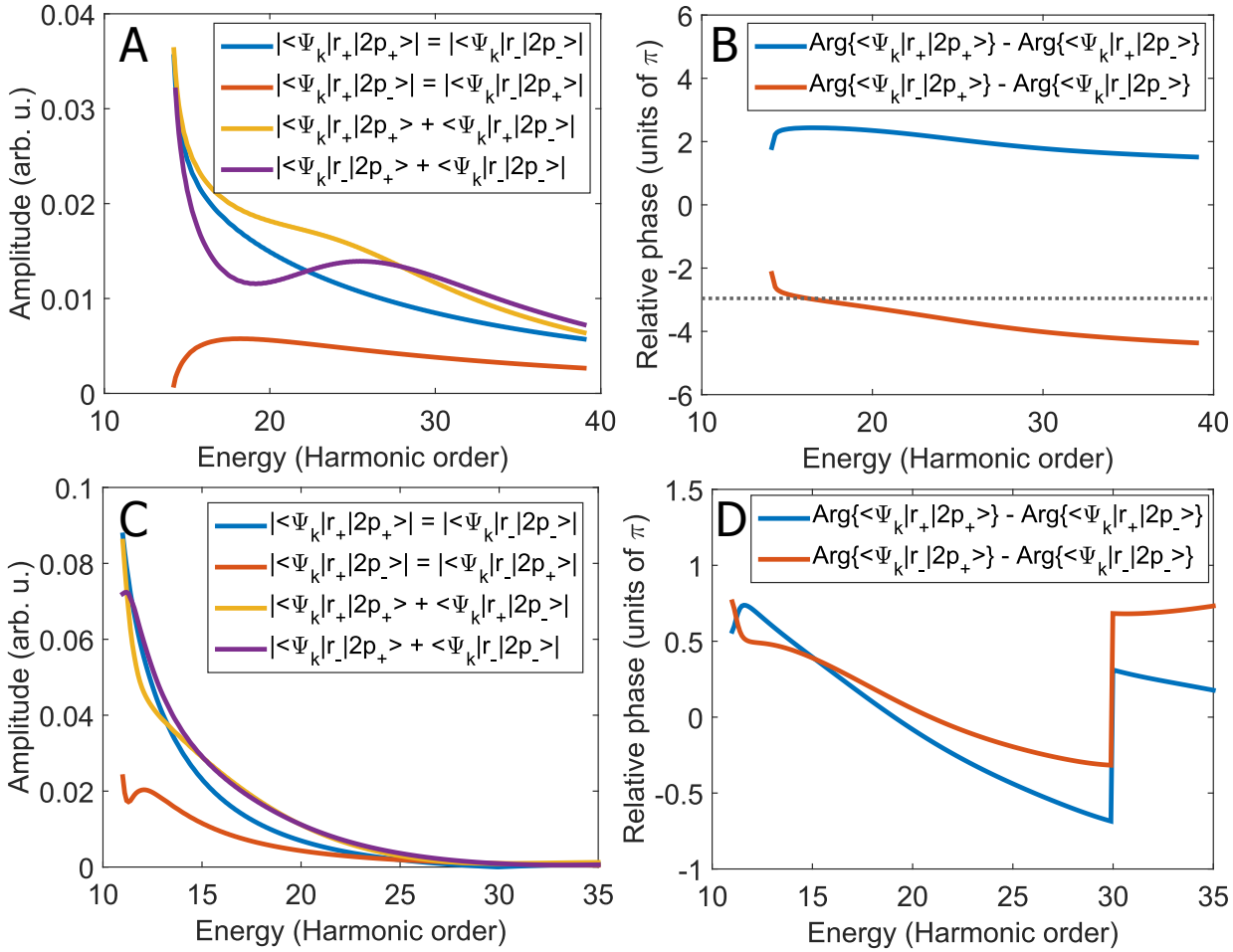

FIG. S5: Panel A: Absolute value of the individual matrix elements $\langle \Psi_{\boldsymbol{k}}^{+} | \hat{r}_{\pm} | 2p_{\pm} \rangle$ as well as their sum for neon. The matrix elements contributing to I_{3q+2} exhibit a suppression around H15-H20. Panel B: Relative phase of the photoionization matrix elements contributing to I_{3q+1} (blue) and I_{3q+2} (red) in Ne. The red curve crosses the value -3π around H17, leading to a destructive interference in the I_{3q+2}-intensity. Panels C and D: Amplitudes and phases of the matrix elements for argon.

Equation (4) suggests that the emission intensity $I_{3q\pm1}$ contains two contributions from matrix elements involving each of the p_+- and p_--orbitals. Examination of eqs. 6-9 reveals that the contributions from the state involving an orbital that is "counter-rotating" with respect to $\hat{r}_{\pm}$ are identical ($\langle \Psi_{\boldsymbol{k}}^{+} | \hat{r}_{-} | 2p_{+} \rangle = \langle \Psi_{\boldsymbol{k}}^{+} | \hat{r}_{+} | 2p_{-} \rangle$). The contributions from the "co-rotating"-orbitals $\langle \Psi_{\boldsymbol{k}}^{+} | \hat{r}_{-} | 2p_{-} \rangle$ and $\langle \Psi_{\boldsymbol{k}}^{+} | \hat{r}_{+} | 2p_{+} \rangle$ are equal in terms of their magnitude, but differ in phase due to the contribution of the angular part mediated by $Y_{2\pm2}(\hat{\boldsymbol{k}})$. In Fig. S5 A

we show the absolute magnitude of the individual $\langle \Psi_{\boldsymbol{k}}^{+} | \hat{r}_{\pm} | 2p_{\pm} \rangle$. The dominance of the "co-rotating" contributions when compared to the "counter-rotating" ones is a manifestation of the "propensity rules" ([14, 15]) in atomic transitions that have been applied in the study of Rydberg atoms in microwave circular fields ([16–18]). Figure S5 B displays the relative phases between the contributions arising from the two orbitals for the $(3q+1)$- ($\langle \hat{r}_{+} \rangle$) and the $(3q+2)$- ($\langle \hat{r}_{-} \rangle$). Whereas the interference between $\langle \Psi_{\boldsymbol{k}}^{+} | \hat{r}_{+} | 2p_{+} \rangle$ and $\langle \Psi_{\boldsymbol{k}}^{+} | \hat{r}_{+} | 2p_{-} \rangle$ remains constructive over the spectral region of interest, the phase difference between $\langle \Psi_{\boldsymbol{k}}^{+} | \hat{r}_{-} | 2p_{+} \rangle$ and $\langle \Psi_{\boldsymbol{k}}^{+} | \hat{r}_{+} | 2p_{+} \rangle$ is close to -3π between H16-H25. As a consequence, a suppression of the I_{3q+2} is expected to occur, in accord with our experimental results. The predicted $I_{3q\pm1}$-intensities for helium, neon and argon are displayed in Fig. S6. As evident from Fig. S6 B, this simplified model reproduces two of the main experimental observations: the suppression of the $(3q+2)$-orders in the region between $H15$ and $H27$ as well as the their subsequent increase after $H28$. The last-mentioned feature is overestimated in this simple model.

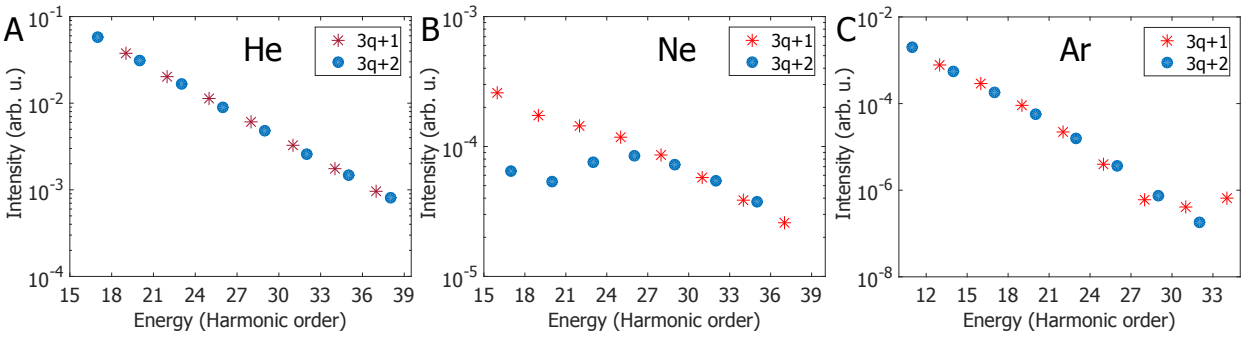

FIG. S6: Estimated relative intensities for the $(3q+1)$- (red stars) vs. $(3q+2)$- (blue circles) harmonic orders for He (panel A), Ne (panel B) and Ar (panel C).

As mentioned in the main text, besides angular momentum symmetry, the ionic potential can also affect the intensity distribution in bicircular HHG. In the case of argon (Fig. S7), the radial parts of the $3p$-photorecombination matrix elements have opposite signs from the ionization threshold (15.76 eV) up to the Cooper minimum (≈ 53 eV) depending on whether the continuum has s- or d-symmetry. Our analysis indicates that this effect counteracts the suppression of the $3q+2$ orders, leading to an intensity distribution similar to that of helium (Fig. S6 C). Figs. S5 C and D display the individual contributions of the matrix elements $\langle \Psi_{\boldsymbol{k}}^{+} | \hat{r}_{\pm} | 2p_{\pm} \rangle$ of Ar and the corresponding phase differences. We note that although this simple model accounts correctly for the relative intensity between adjacent members

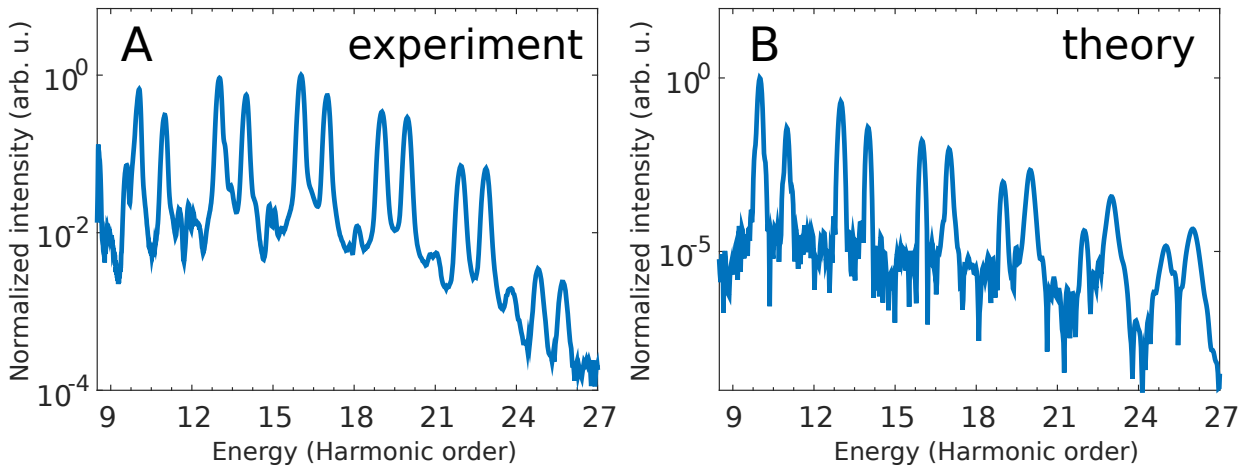

FIG. S7: Panel A: Experimental HHG spectrum of argon in the bicircular configuration (logarithmic scale). Panel B: TDSE calculation of the harmonic emission in Ar corresponding to the experimental conditions in A ($I_\omega = 2.0 \times 10^{14}\mathrm{W/cm}^2$, $I_{2\omega} = 0.5 \times 10^{14}\mathrm{W/cm}^2$).

of a given $3q + 1/3q + 2$-pair, the overall intensity distribution is not well reproduced. The disagreement is most prominent in the low-energy part of the spectrum, where recollision-based theories cannot be expected to be accurate. For completeness, we show in Fig. S7 B the TDSE simulation of BHHS in argon. The scale in Figs. S7 A and B is logarithmic in order to facilitate the comparison between experimental and theoretical results. Overall, the $3q + 1/3q + 2$-ratios are correctly reproduced in the range $H9 - H18$ but the theory overestimates the contribution of the $3q + 2$-member in the cutoff-region.

IV. RECOMBINATION STEP IN BHHS OF MOLECULES

A. Isotropic ensemble

The Z-axis of the laboratory frame is chosen to coincide with the photon propagation direction, i. e. $Z \parallel \hat{\boldsymbol{n}}$. The electron trajectory is characterized by the recombination angle ϕ_k, measured with respect to the laboratory X-axis. The values of ϕ_k are obtained with the saddle-point-method introduced in the preceding section. We stress that this approach does not take the angular dependence of the ionization step into account. We restrict our analysis to motion within the XY (lab)-plane, thus the recombination trajectory is given by $\hat{k}_\mathrm{L} = (\theta_k = \pi/2,\, \phi_k)$. Let α, β, γ be the Euler angles such that the rotation $\mathcal{D}(\alpha,\, \beta,\, \gamma)$

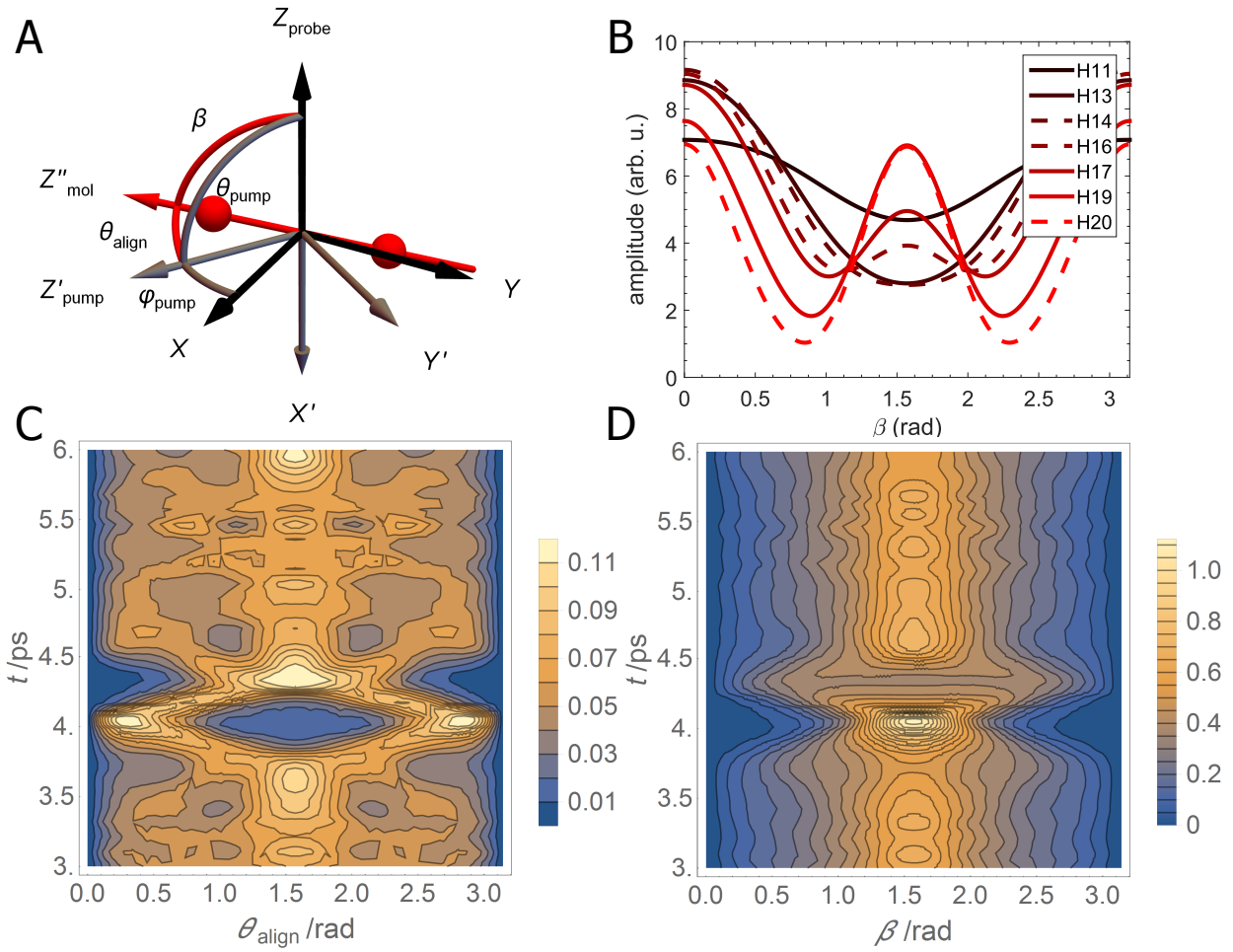

FIG. S8: Panel A: Relation between the various coordinate systems discussed in the text. Unprimed letters pertain to the laboratory frame, primed ones define the "pump frame". In the calculations, we employ $Z' \parallel X$, here both vectors are offset by ϕ_{pump} for clarity. The red axis defines the molecular-frame Z''_{mol}-axis, whose orientation is specified by $(\vartheta_{\text{align}}, \varphi_{\text{align}})$ in the pump frame and (β, α) in the lab frame. α is not shown. Panel B: Photorecombination matrix elements with respect to the lab frame for various harmonic orders, averaged over one cycle assuming an isotropic distribution. Panel C: Calculated alignment distribution $A(\vartheta_{\text{align}}) \sin \vartheta_{\text{align}}$ in the pump frame. Panel D: Calculated alignment distribution $A'(\beta) \sin \beta$, transformed to the lab frame and averaged over the azimuthal angle α.

transfers the lab frame (LF) into the molecular frame (MF). In particular, α and β represent the azimuthal and the polar angle of the molecular z-axis in the LF (cp. Fig. S8 for the definition of the various coordinate systems). The photorecombination matrix element in

the MF can be obtained in terms of the partial-wave matrix elements $I_{lm\mu}$ using the relation:

$$T_{f\leftarrow i} = \sqrt{\frac{4\pi}{3}} \sum_{lm\mu} I_{lm\mu} Y^*_{lm}(\hat{k}_{\mathrm{M}}) Y^*_{1\mu}(\hat{n}_{\mathrm{M}}). \tag{10}$$

The quantities $I_{lm\mu}$ are caculated with the ePolyScat code ([19, 20]). $\hat{k}_{\mathrm{M}}$ is the recombining electron trajectory in the MF, its value is known the lab frame. We can express $T_{f\leftarrow i}$ in the LF by:

$$T^{(\mathrm{LF})}_{f\leftarrow i}(\alpha,\,\beta,\,\gamma) = \sqrt{\frac{4\pi}{3}} \sum_{lm\mu} I_{lm\mu} \sum_{m'=-l}^{l} \mathcal{D}^{l}_{m',m}(\alpha,\,\beta,\,\gamma) Y^*_{lm'}(\hat{k}_{\mathrm{L}}) \sum_{\mu'=-1}^{1} \mathcal{D}^{1}_{\mu',\mu}(\alpha,\,\beta,\,\gamma) Y^*_{1\mu'}(\hat{n}_{\mathrm{L}}). \tag{11}$$

This event repeats itself three times each cycle, the individual trajectories are spaced by $\Delta\phi = \frac{2\pi}{3}$ in angular space and by a phase factor of $N\frac{2\pi}{3}$ in time (N is the harmonic order). Adding the three bursts vectorially in the lab frame gives the following result for the clockwise/counter-clockwise helicity:

$$\begin{aligned} T^{(\mathrm{LF})}_{f\leftarrow i}(\alpha,\,\beta,\,\gamma) = \sqrt{\frac{4\pi}{3}} \sum_{j=-1}^{j=+1} \sum_{lm\mu} I_{lm\mu} \sum_{m'=-l}^{l} \sum_{\mu'=-1}^{1} \mathcal{D}^{l}_{m',m}(\alpha,\,\beta,\,\gamma) Y^*_{lm'}(\tfrac{\pi}{2}, \phi_k + j\tfrac{2\pi}{3}) \times \\ \mathcal{D}^{1}_{\mu',\mu}(\alpha,\,\beta,\,\gamma) Y^*_{1\mu'}(\tfrac{\pi}{2}, \phi_k + j\tfrac{2\pi}{3}) \left(\cos(\phi_k + j\tfrac{2\pi}{3})\hat{x}_{\mathrm{L}} \pm \iota \sin(\phi_k + j\tfrac{2\pi}{3})\hat{y}_{\mathrm{L}}\right) \mathrm{e}^{\iota j N \frac{2\pi}{3}}. \end{aligned} \tag{12}$$

The total intensity is obtained after coherent integration over all orientations:

$$I_{f\leftarrow i} = \left| \int_0^{2\pi} \mathrm{d}\alpha \int_0^{2\pi} \mathrm{d}\gamma \int_0^{\pi} \mathrm{d}\beta T^{(\mathrm{LF})}_{f\leftarrow i}(\alpha,\,\beta,\,\gamma) \sin\beta \right|^2. \tag{13}$$

For $N = 3k, k \in \mathbb{N}_+$, (12) vanishes.

B. Aligned ensemble

Equation (12) is generally valid. The problem is how to set the Euler angles. The easiest way is to introduce an intermediate "pump" system denoted by primed symbols (X', Y', Z'). Z' is the pump polarization axis and we set $Z' \parallel X$. This means that the X-lab-axis is now defined by the pump axis. Let $(\vartheta_{\mathrm{align}}, \varphi_{\mathrm{align}})$ define the molecular orientation with respect to the pump frame for a linear molecule. The angle distribution function in this frame is isotropic with respect to φ_{align}, $A(\vartheta_{\mathrm{align}}, \varphi_{\mathrm{align}}) \to A(\vartheta_{\mathrm{align}})$. If the pump frame is tilted by an angle θ_{pump} with respect to the lab frame (here $\theta_{\mathrm{pump}} = \pi/2$), the molecular distribution in the lab frame can be obtained using the cosine theorem as:

$$A'(\beta, \alpha) = A(\vartheta_{\mathrm{align}}(\beta, \alpha)) = A\big(\arccos(\cos\alpha \sin\beta)\big). \tag{14}$$

The alignment distribution is obtained from a rotational TDSE-calculation ([21]) assuming a pump pulse of intensity $I = 7 \times 10^{13}\mathrm{W/cm}^2$, a pulse duration of 60 fs and a rotational temperature of 25 K. The intensity is obtained by weighting (12) with the axis distribution:

$$I_{f\leftarrow i} = |\int_0^{2\pi} \mathrm{d}\alpha \int_0^{\pi} \mathrm{d}\beta A'(\beta,\alpha) T_{f\leftarrow i}^{(\mathrm{LF})}(\alpha,\beta,\gamma=0)\sin\beta|^2, \tag{15}$$

since γ can be set arbitrarily for a linear molecule. In the above, we have assumed that $Z' \parallel X$. This assumption implicitly requires that the phase delay between the fundamental and its second harmonic ($\Delta\varphi$) is known. Since interferometric stability cold not be achieved in our optical setup, the results presented in S8 are calculated for many $\Delta\varphi$ between 0 and 2π and subsequently averaged.

---

[1] O. Kfir et al., Nature Photonics **9**, 99 (2015).

[2] M. D. Morse, *Experimental Methods in Physical Sciences*, volume 29 of *Atomic, Molecular, and Optical Physics: Atoms and Molecules Part B*, chapter 2, pages 21–47, Elsevier Inc., 1996.

[3] A. Börzsönyi, Z. Heiner, M. P. Kalashnikov, A. P. Kovács, and K. Osvay, Appl. Opt. **47**, 4856 (2008).

[4] E. Constant et al., Phys. Rev. Lett. **82**, 1668 (1999).

[5] T. Popmintchev et al., Proceedings of the National Academy of Sciences **106**, 10516 (2009).

[6] T. Popmintchev et al., Science **336**, 1287 (2012).

[7] J. Samson and W. Stolte, Journal of Electron Spectroscopy and Related Phenomena **123**, 265 (2002), Determination of cross-sections and momentum profiles of atoms, molecules and condensed matter.

[8] X.-M. Tong and S.-I. Chu, Chemical Physics **217**, 119 (1997), Dynamics of Driven Quantum Systems.

[9] M. Murakami, O. Korobkin, and M. Horbatsch, Phys. Rev. A **88**, 063419 (2013).

[10] X. M. Tong and C. D. Lin, Journal of Physics B: Atomic, Molecular and Optical Physics **38**, 2593 (2005).

[11] H. G. Muller and F. C. Kooiman, Phys. Rev. Lett. **81**, 1207 (1998).

[12] H. J. Wörner, H. Niikura, J. B. Bertrand, P. B. Corkum, and D. M. Villeneuve, Phys. Rev. Lett. **102**, 103901 (2009).

[13] D. B. Milošević, W. Becker, and R. Kopold, Phys. Rev. A **61**, 063403 (2000).

[14] H. A. Bethe and E. E. Salpeter, *Quantum Mechanics of One- and Two-Electron Atoms*, Springer US, 1977.

[15] U. Fano, Phys. Rev. A **32**, 617 (1985).

[16] J. Zakrzewski, D. Delande, J.-C. Gay, and K. Rzążewski, Phys. Rev. A **47**, R2468 (1993).

[17] K. Rzążewski and B. Piraux, Phys. Rev. A **47**, R1612 (1993).

[18] D. Farrelly and T. Uzer, Phys. Rev. Lett. **74**, 1720 (1995).

[19] F. A. Gianturco, R. R. Lucchese, and N. Sanna, The Journal of Chemical Physics **100**, 6464 (1994).

[20] A. P. P. Natalense and R. R. Lucchese, The Journal of Chemical Physics **111**, 5344 (1999).

[21] J. Ortigoso, M. Rodríguez, M. Gupta, and B. Friedrich, The Journal of Chemical Physics **110**, 3870 (1999).